Photon-counting computed tomography of lanthanide contrast agents with a high-flux 330-μm-pitch cadmium zinc telluride detector in a table-top system

Chelsea A. S. Dunning,[a,*] Jericho O'Connell,[a] Spencer M. Robinson,[a] Kevin J. Murphy,[a] Adriaan L. Frencken,[b,c] Frank C. J. M. van Veggel,[b,c] Kris Iniewski,[d] and Magdalena Bazalova-Carter[a]

[a]University of Victoria, Department of Physics and Astronomy, Victoria, British Columbia, Canada

[b]University of Victoria, Department of Chemistry, Victoria, British Columbia, Canada

[c]University of Victoria, CAMTEC, Centre for Advanced Materials and Related Technologies, Victoria, British Columbia, Canada

[d]Redlen Technologies, Saanichton, British Columbia, Canada

Abstract

Purpose: We present photon-counting computed tomography (PCCT) imaging of contrast agent triplets similar in atomic number (Z) achieved with a high-flux cadmium zinc telluride (CZT) detector.

Approach: The table-top PCCT imaging system included a 330-μm-pitch CZT detector of size 8 mm $\times$ 24 mm^2 capable of using six energy bins. Four 3D-printed 3-cm-diameter phantoms each contained seven 6-mm-diameter vials with water and low and high concentration solutions of various contrast agents. Lanthanum ($Z = 57$), gadolinium (Gd) ($Z = 64$), and lutetium ($Z = 71$) were imaged together and so were iodine ($Z = 53$), Gd, and holmium ($Z = 67$). Each phantom was imaged with 1-mm aluminum-filtered 120-kVp cone beam x rays to produce six energy-binned computed tomography (CT) images.

Results: K-edge images were reconstructed using a weighted sum of six CT images, which distinguished each contrast agent with a root-mean-square error (RMSE) of <0.29% and 0.51% for the 0.5% and 5% concentrations, respectively. Minimal cross-contamination in each K-edge image was seen, with RMSE values <0.27% in vials with no contrast.

Conclusion: This is the first preliminary demonstration of simultaneously imaging three similar Z contrast agents with a difference in Z as low as 3.

 [DOI: 10.1117/1.JMI.7.3.033502]

Keywords: contrast agents; multienergy computed tomography; image reconstruction; photon-counting detectors; lanthanides.

Paper 19314RR received Dec. 8, 2019; accepted for publication May 20, 2020; published online Jun. 15, 2020.

1 Introduction

Computed tomography (CT) is a widely available clinical imaging modality that conventionally uses diagnostic x-rays for the purpose of visualizing patient anatomy. The use of energy-selective x-ray CT for material analysis was proposed in the 1970s.[1] Energy-selective CT imaging is widely applied in the form of dual-energy CT (DECT) imaging in which the effective atomic number (Z) of each material can be reconstructed and used for a more accurate material analysis compared to conventional x ray CT that only offers attenuation information. DECT, like conventional CT imaging, uses energy-integrated detectors that measure photon flux. Many studies have employed DECT for the purpose of distinguishing contrast material, such as iodine (I), from a

*Address all correspondence to Chelsea A. S. Dunning, E-mail: cdunning@uvic.ca

2329-4302/2020/$28.00 © 2020 SPIE

wide range of organs[2] and to aid in diagnoses of anomalies, such as urinary stones, pulmonary embolisms, and thyroid lesions.[3–5] Clinical DECT can be performed by either scanning with two different x ray tube voltages to create two separate images or by scanning with a single tube voltage to create two images from energies above and below the *K*-edge of the material, which are then postprocessed to enhance the material of interest. These two methods present a number of challenges in terms of imaging setup, scatter, and/or imaging dose. In addition, DECT is often limited to distinguishing materials with very different attenuation curves, such as bone and soft tissue.[6] Due to the recent advancements in photon-counting detector development, multienergy x-ray imaging, or photon-counting CT (PCCT), has become possible. Photon-counting detectors are based on the concept that incoming photons are counted and spectrally binned by analyzing the pulse heights generated in a semiconductor detection layer. PCCT imaging is capable of distinguishing multiple high-*Z* materials by selecting appropriate energy bins above and below the *K*-edges of each material on a detector capable of energy discrimination. In DECT imaging, a similar effect is achieved by selecting appropriate x-ray beam energies on either side of a *K*-edge for one material.[7] The main advantage of PCCT when combined with K-edge imaging is the ability to discern high-*Z* materials from structures such as bone, which would be difficult to resolve in a conventional energy-integrated CT image. As demonstrated in the Monte Carlo study by Bazalova et al.,[8] gold and platinum were easily separated independently from two types of bone material with similar CT numbers in a *K*-edge subtracted image using a pencil beam of 110-kVp x-rays. *K*-edge subtracted imaging is also simpler to implement compared to basic material decomposition.

Previously, a photon-counting detector was used to image the abdominal area in humans containing I without compromising image quality in the CT image offered by a conventional energy-integrating detector, which demonstrated the ease of translating PCCT to the clinic.[9] Further use of photon-counting detectors in PCCT imaging for large animal and human subjects[10,11] also demonstrates this clinical translation. PCCT creates a paradigm shift in the clinical routine as it enables differentiation between two or more contrast agents in a single CT acquisition via *K*-edge imaging. In the case of CT colonography, for example, one contrast agent could be administered intravenously for enhancement of polyps, and a second contrast agent could be administered orally for tagging fecal material and residual fluid in the bowel. In this example, the feasibility of using PCCT to differentiate between gadolinium (Gd) and iodine-based contrast material in a colon phantom was investigated using the characteristic *K*-edge of Gd.[12] Imaging three contrast agents could enable the diagnosis of inflammatory diseases, as well as monitoring drug delivery and the immune response to the drug in cancer treatment in the same scan.[13] However, the inability of photon-counting detectors to sustain high photon fluxes causes PCCT to lag behind conventional photon-integrating x-ray CT imaging.

One goal of this study was to simultaneously image three high-*Z* contrast agents with a high-flux photon-counting detector using *K*-edge subtraction techniques and to explore the limitation of PCCT when imaging contrast agents that are similar in *Z*. Two of the five elements considered, namely I and Gd, are used clinically. I is a routinely used contrast agent for many clinical DECT scans to diagnose a wide range of diseases.[7,14] However, its low *K*-edge energy of 33.2 keV makes it difficult for *K*-edge imaging. Gd, while typically used as a contrast agent in magnetic resonance imaging (MRI) scans, has also been shown to enhance lung and kidney vasculature in CT imaging[15] and has been used as a contrast agent for other PCCT studies.[16–19] The group of elements known as the lanthanides, which include Gd, lanthanum (La), lutetium (Lu), and holmium (Ho), is being recognized as alternative contrast agents. Lanthanum carbonate, in particular, is effective as a way to lower excessive phosphate levels in kidney disease.[20] Lu has shown promise as a sensitizer for photodynamic therapy of prostate cancer.[21] Ho, while not commonly used in biological applications, may be a candidate as a high-field MRI contrast agent.[22] Elements with *Z*s between 56 and 73, which include the lanthanides, were demonstrated to have the best contrast enhancement for CT images using energies between 80 and 140 kVp.[23] PCCT experiments and simulations imaging ytterbium, hafnium, and other nearby elements, such as osmium, europium, and thallium, have been successful in identifying these elements.[24–26] However, as far as we know, PCCT imaging of La, Lu, and Ho has never been investigated.

PCCT imaging has been successfully used to simultaneously image Gd and I contrast agents using the Medipix silicon spectral detector[17] and a cadmium telluride (CdTe) detector array.[27] Simultaneous PCCT imaging of three contrast agents was achieved using four optimized energy bins on a photon-counting detector with a CdTe sensor (MARS Bioimaging, Christchurch, New Zealand).[28,29] However, due to the lower absorption efficiency of silicon at higher x-ray energies compared to CdTe and cadmium zinc telluride (CdZnTe, hereafter referred to as CZT), the silicon-based detector may struggle to image higher-Z materials with similar detector thicknesses. CdTe detectors, compared to CZT, have a narrower bandgap, which leads to a lower resistivity and higher leakage current noise.[30] The most recent PCCT prototype scanners use CZT as a sensor material for this reason. Si-Mohamed et al.[31] used PCCT to simultaneously generate I and Gd maps *in vivo* for a tumor model in a rabbit liver. The present study used a high-flux, photon-counting CZT detector on a table-top cone beam system. We demonstrate the first simultaneous PCCT of three elements similar in Z using K-edge subtraction inside a small phantom.

2 Methods

2.1 *Imaging Setup and Phantom*

The imaging setup consisted of an x-ray tube, a CZT detector, linear motion stages, a rotation stage, and the phantom [Fig. 1(a)]. The CZT detector (Redlen Technologies, Saanichton, BC, Canada) consisted of two adjacent modules each 8×12 mm^2 in size with a 2-mm thick, 330-μm pitch high-flux sensor. The modules were oriented such that the total active area of the detector was 8 mm $\times$ 24 mm^2. The sensor was capable of operating at 250 Mcps/mm^2 rates without any signs of polarization.[32] The MRX-160/22 x-ray tube (Comet Technologies, Flamatt, Switzerland) and the CZT detector were mounted on the M-IMS300V and M-IMS600LM motion stages, and the phantom rested on an RVS80CC rotation stage on an optical table (Newport Corporation, Irvine, CA).

The 3D-printed cylindrical phantoms used in this study were 3 cm in diameter and 2.5 cm in height and made of solid polyactic acid of density 1.25 g/cm^3 (Conceptualize CAD & Print, Victoria, BC, Canada). Seven holes of diameter 0.6 cm were built into the phantom to allow a snug fit for inserting 0.2-mL flat cap tapered plastic tubes (Fisher Scientific, Ottawa, Ontario, Canada). One hole was at the phantom center, and the other six were located on a 9-mm-radius circle concentric with the phantom. These tubes, hereafter referred to as vials, contained various triplet combinations of contrast agents whose concentrations by weight were arranged as shown in Figs. 1(b)–1(e) to form four distinct phantoms. The phantoms containing 1% to 5% and 0.5% to 3% La, Gd, and Lu solutions are referred to as the high concentration (HC) and

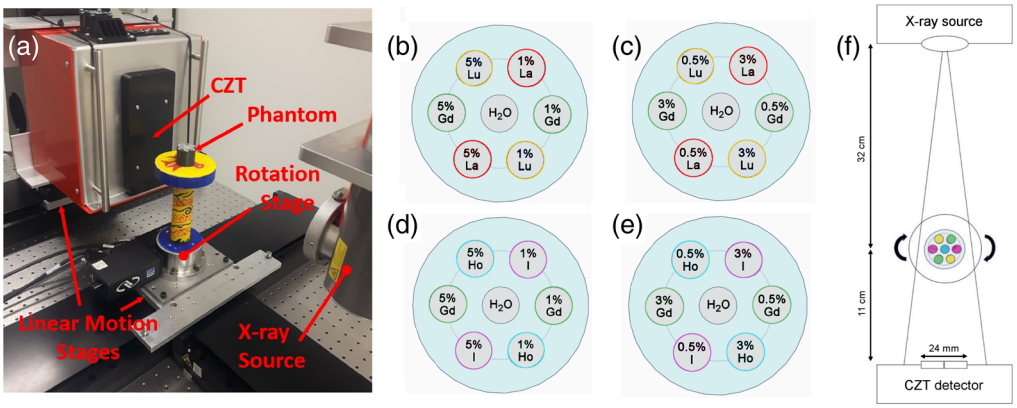

Fig. 1 (a) Lab setup for PCCT data acquisitions with components labeled. Contrast phantom depicting layout of concentrations for (b) HC and (c) LC La, Gd, and Lu, and (d) HC and (e) LC I, Gd, and Ho in each vial. (f) Schematic diagram showing the PCCT imaging setup.

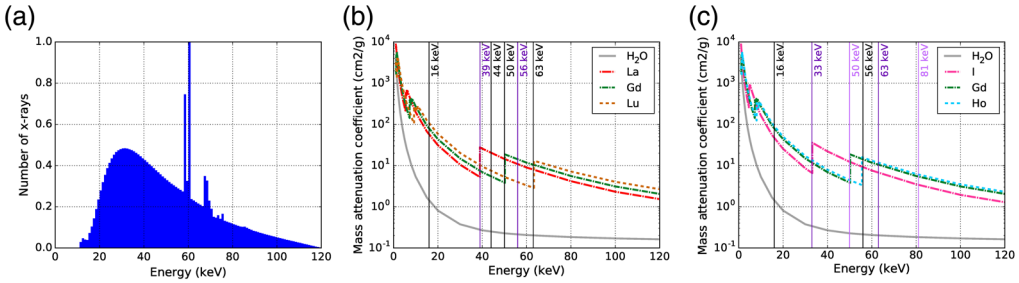

Fig. 2 (a) Spectrum of 120-kVp x-ray beam filtered with 1-mm Al and collimated by lead, which adds features including increased attenuation below the *L*-edges of lead and *K*-shell fluorescence x-rays from lead. Mass attenuation coefficients[33] of (b) La, Gd, Lu and (c) I, Gd, and Ho plus water shown with the thresholds of the energy bins on the CZT detector for each phantom.

low concentration (LC) La–Gd–Lu phantoms, respectively, and are shown in Figs. 1(b) and 1(c). Figures 1(d) and 1(e) show the phantoms containing 1% to 5% and 0.5% to 3% I, Gd, and Ho solutions and are referred to as the HC and LC I–Gd–Ho phantoms, respectively. The I solution used was iodine-based Omnipaque 300 (iohexol, GE Healthcare, Princeton, New Jersey, USA) diluted in deionized water. The La, Gd, Lu, and Ho contrast agents for the La–Gd–Lu and I–Gd–Ho phantoms were in the form of lanthanum (III) chloride heptahydrate (≥99.999%), gadolinium (III) chloride hexahydrate (99.999%), holmium (III) chloride hexahydrate (99.9%), and lutetium (III) chloride hexahydrate (≥99.99%) dissolved in deionized water, respectively (Sigma-Aldrich, Oakville, Ontario, Canada).

Each phantom was imaged using a cone beam CT geometry with the setup shown in Fig. 1(f). The x-ray beam was collimated with lead such that the beam area at the isocenter was 36.6 mm in width and 13.7 mm in height. The beam spectrum shown in Fig. 2(a) was simulated using an existing Monte Carlo model of the x-ray tube.[34]

2.2 *Photon-Counting Detector*

The detector consisted of integrated readout electronics with a CZT sensor. The CZT crystal was grown using the traveler heat method (Redlen Technologies, Saanichton, British Columbia) and was chosen over CdTe due to its superior quantum efficiency. The CZT sensor had 864 individual pixels (24×36) with a pixel count variability of <10% and an individual pixel energy resolution of 6 to 9 keV. As specified by the manufacturer, the CZT detector performed a spectral sweep of ^{241}Am to measure the energy resolution. The full-width at half-maximum (FWHM) of the 59.5-keV gamma ray peak of ^{241}Am was 8.9 keV. The sensor was connected to the high-speed photon-counting application-specific integrated circuit (ASIC) that operated at rates up to 62.5 million counts per second per channel with six energy bin configurations. The ASIC communicated through high-speed low-voltage differential signaling input/outputs to the external computer via a field-programmable gate array. The energy of photons incident onto the detector was sorted into six energy bins, which were adjustable in the 16- to 200-keV energy range. The choice of thresholds forming the six energy bins to coincide with the *K*-edges of the each contrast agent in each phantom enabled simultaneous, multiplexed K-edge imaging. The mass attenuation coefficients of each contrast agent, including their *K*-edge energy values, and the energy bin thresholds for each phantom scan are shown in Figs. 2(b) and 2(c).

2.2.1 *Energy bin settings*

For the HC and LC La–Gd–Lu phantoms, the energy bins on the CZT detector were set to accommodate for the K-edge values of La, Gd, and Lu. The intermediate thresholds of 44 and 56 keV were chosen such that there was an equal amount of x-rays in each energy bin using the x-ray beam spectrum in Fig. 2(a). For the HC and LC I–Gd–Ho phantoms, the energy bins were set to accommodate the *K*-edge values of I, Gd, and Ho. Table 1 summarizes the *K*-edge energies of each element in all phantoms and the detector energy thresholds used for each acquisition.

Table 1 Summary of *K*-edge energies of each element and detector energy thresholds.

Phantom	La–Gd–Lu			I–Gd–Ho		
Element	La	Gd	Lu	I	Gd	Ho
K-edge energy (keV)	38.9	50.2	63.3	33.2	50.2	55.6
CZT energy thresholds (keV)	16, 39, 44, 50, 56, 63, 120			16, 33, 50, 56, 63, 81, 120		

2.3 *Data Acquisition*

For all scans of each phantom, 180 projections were acquired over a 360-deg continuous rotation at a speed of 1.48 deg per second about the isocenter. Three rotations were performed in order to image across the entire phantom body 3 cm in diameter. Because the linear motion stages allowed for submillimeter accuracy in motion of the detector and x-ray source, stitching of each projection produced from the three 360-deg rotations together was possible. The x-ray source was running at 120 kVp and 1 mA with a 1-mm focal spot and 1 mm of aluminum filtration. The detector acquired projection data over 0.25 s intervals every 1 s, with an approximate data saving time of 0.34 s per projection. The acquisition time for one full rotation of the phantom was 4 min, so with three full rotations it took 12 min to image the whole phantom.

2.4 *Image Reconstruction*

2.4.1 *PCCT image reconstruction*

All of the projection data, including the air and dark field scans, were corrected for bad pixel response using nearest-neighbor pixel interpolation.[29] Detector counts in each energy bin were converted into projections p in the following manner:

$$p = -\ln[(I - I_{\text{dark}})/(I_0 - I_{\text{dark}})], \tag{1}$$

where I is the detector signal with the phantom, I_0 is the detector signal without the phantom, and I_{dark} is the detector signal with no beam. For the different energy bins, the projection data from each detector translation were stitched together to generate projections of the entire phantom. All images underwent ring-artifact corrections using the wavelet-FFT method,[35] which used a DB42 wavelet with a third-level decomposition and a damping coefficient of 1.2. The CT images were then reconstructed using the Feldkamp–Davis–Kress algorithm[36] with a Hamming filter. The resulting CT images at each energy bin were 129×129 pixels in size, and the reconstructed cubic voxel size was 250 μm. MATLAB® (The Mathworks, Natick, Massachusetts, USA) was used for data processing and image reconstruction, while Python was used for data analysis.

2.4.2 *K-edge images*

In general, a *K*-edge image for a given contrast agent can be reconstructed by subtracting the CT image of the energy bin directly above the *K*-edge from the CT image directly below the *K*-edge. In this study, the *K*-edge images were reconstructed using a weighted sum of all energy binned CT images in the following manner:

$$y_X = \sum_{i=1}^{6} w_{Xi} a_i, \tag{2}$$

where y_X is the K-edge image of contrast agent X, a_i is the CT image at bin i, and w_{Xi} is the weight given to bin i. The weight w_{Xi} is a number that is constrained between -1 and 1. The known concentrations of the HC phantoms were used to find the weights using a minimization algorithm and then applied to the LC phantoms. In this algorithm, the COBYLA method[37] was

used with an error tolerance of 1×10^{-8}, bounds of -1 and 1, and 100 maximum iterations to find the weights w_{Xi} that would give the minimum value of $|y_X - u_X|$. Here, u_X is the ground truth K-edge image of contrast agent X. The initial guess of weights to initiate the optimization were set manually to obtain the best images. Once the weights were found for the K-edge images of the contrast agents in the HC phantoms, the same weights were applied in Eq. (2) to form the K-edge images of the contrast agents in the LC phantoms. This was done to validate the weights on an independent phantom scan. All K-edge images were scaled to a 5% contrast in the respective HC phantom, and a single slice for each K-edge image was selected for presentation. Negative values arising from Eq. (2) subtraction in the zero-contrast vials were set to 0. The minimization algorithm was available in the SciPy Optimize package.[38]

2.4.3 *Signal linearity*

The linearity of the contrast agent signal from each vial was assessed by comparing the reconstructed concentrations in each K-edge image to the actual concentration. Error bars for the reconstructed concentration were calculated to be the standard deviation of the pixels in the region of interest (ROI). The difference of concentration for each vial was found by subtracting the actual concentration from the reconstructed concentration. The signal and error of 0% contrast were calculated as the average and standard deviation, respectively, of all peripheral zero-contrast vials in both the HC and LC K-edge images. Each data set was fit to a linear function with the y intercept fixed at zero, and an R^2 value was found to assess the goodness of fit. The slope and its associated error of the linear function was found with a curve fit algorithm available in the SciPy Optimize package.[38]

2.4.4 *Root-mean-square error*

We used the root-mean-square error (RMSE) to quantify the quality of the contrast agent separation. The RMSE in each K-edge image was evaluated for an ROI containing n pixels by the following:

$$\mathrm{RMSE} = \sqrt{\frac{\sum_{j=1}^{n} (\hat{y}_j - y_j)^2}{n}}, \tag{3}$$

where $\hat{y}_j$ and y_j are the expected and measured values, respectively, in pixel j of a K-edge image. Each ROI was centered on a 6-mm-diameter vial and was defined as a 4-mm-diameter circle. The expected value in the nonzero contrast vials should be equal to the concentration of the contrast agent. The expected value in each of the zero-contrast ROIs should be 0, and a high RMSE value should indicate a large amount of cross contamination from these vials. The calculated RMSE for the ROI over the middle water vial was omitted due to ring artifacts that were found to obscure the signal.

2.5 *Dose Estimation*

To estimate the dose of the PCCT scan, a 3-cm-diameter circle was cut out of a sheet of Gafchromic® EBT3 film (Ashland Advanced Materials, Bridgewater, New Jersey, USA) and irradiated at its isocenter between two 3-cm-diameter cylindrical phantoms with water vials using the same imaging setup. The calibration curve was generated using doses between 0.2 and 8 Gy measured with a Farmer-type ion chamber calibrated in a kilovoltage beam according to the procedure outlined in Ref. 34 using an x-ray tube voltage of 120 kVp with 1-mm Al filtration. Irradiated films were scanned 24 h after exposure with an EPSON® 10000XL flatbed scanner (Epson America, Long Beach, California, USA) at a resolution of 200 dots per inch, and FilmQA pro® (Ashland Advanced Materials, Bridgewater, New Jersey, USA) was used to analyze the films using triple-channel dosimetry. The phantom dose was estimated by calculating the optical density in a 2×2 cm^2 region in the middle of the film. The imaging dose was calculated from the proportion of the actual beam-on time for a 0.25-s acquisition.

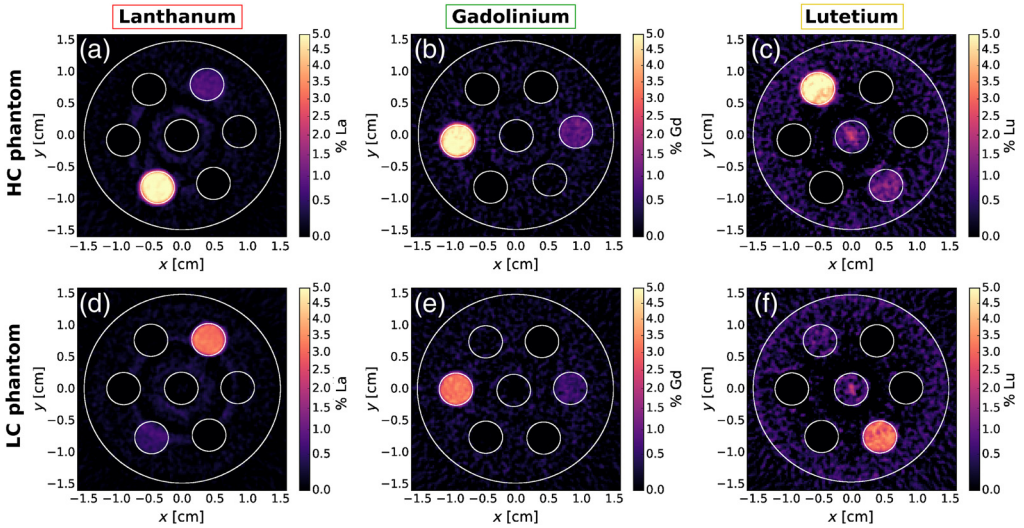

Fig. 3 *K*-edge images of the HC and LC La–Gd–Lu phantoms showing contrast for (a), (d) La; (b), (e) Gd; and (c), (f) Lu.

3 Results

3.1 *K-Edge Images*

Figure 3 shows the results of the *K*-edge subtraction technique for La, Gd, and Lu, respectively, for the HC and LC phantoms. Figure 4 shows the results of the *K*-edge subtraction technique for I, Gd, and Ho, respectively. The weights w_i from Eq. (2) used for *K*-edge reconstruction of the La–Gd–Lu and I–Gd–Ho phantoms are shown in Tables 2 and 3, respectively. Both La and Lu, each having a difference in Z of 7 from Gd, stood out from Gd in the *K*-edge images. There was good contrast agent discrimination for all vials in each *K*-edge image of the LC and HC phantoms except the 0.5% vial was difficult to resolve for Lu. There was some false signal in the middle of the Lu image due to ring artifacts in the CT images and the narrow energy bins set by the detector. The I *K*-edge images in Figs. 4(a) and 4(d) had excellent contrast agent discrimination. As shown in Figs. 4(b) and 4(e) for Gd and Figs. 4(c) and 4(f) for Ho, these contrasts with a difference in Z of 3 were discriminated from each other. Some false signal was evident in and

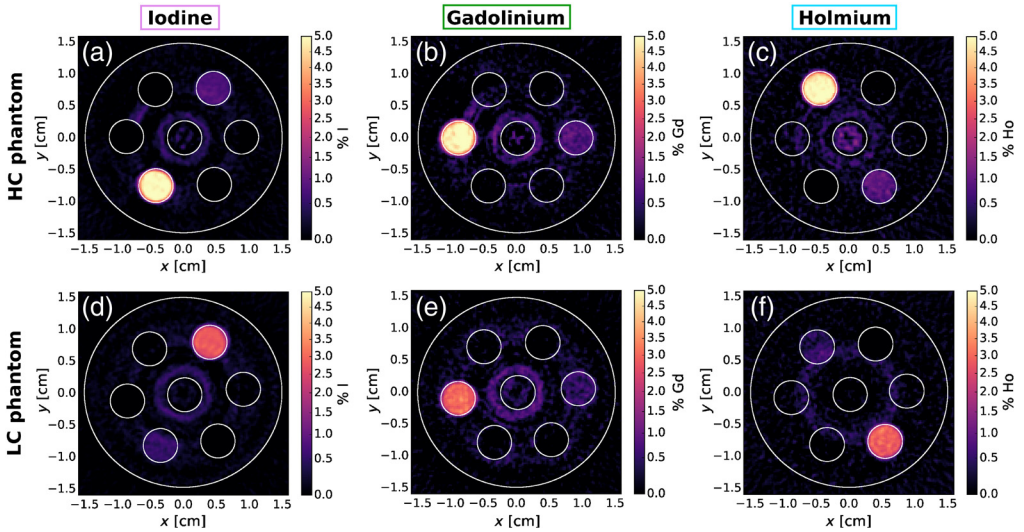

Fig. 4 *K*-edge images of the HC and LC I–Gd–Ho phantoms showing contrast for (a), (d) I; (b), (e) Gd; and (c), (f) Ho.

Table 2 Weights of energy-binned CT images to form La–Gd–Lu phantom *K*-edge images.

Contrast agent	w_1	w_2	w_3	w_4	w_5	w_6
La	−0.740	0.933	0.005	0.081	−0.016	−0.125
Gd	0.011	0.012	−0.975	0.980	−0.005	0.034
Lu	−0.030	−0.029	0.031	0.098	−1.105	0.967

Table 3 Weights of binned CT images to form I–Gd–Ho phantom *K*-edge images.

Contrast agent	w_1	w_2	w_3	w_4	w_5	w_6
I	−0.753	0.984	−0.034	0.088	−0.129	0.002
Gd	−0.723	−0.011	0.949	−0.019	0.039	0.024
Ho	0.006	0.058	−0.956	0.956	0.007	−0.013

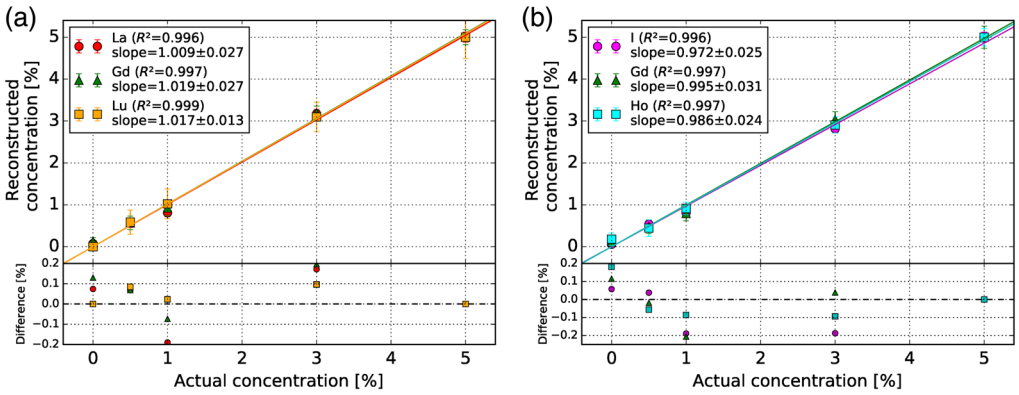

Fig. 5 Reconstructed versus actual concentration of each contrast agent in the (a) La–Gd–Lu and (b) I–Gd–Ho phantoms. The slope and the R^2 value of the fitted data are shown in the legend. The subplot shows the difference between the reconstructed and actual concentrations.

around the middle water vial in these Ho and Gd *K*-edge images, likely due to ring artifacts that were present in the CT images.

3.2 *Evaluation of K-Edge Images*

3.2.1 *Reconstructed concentration*

The reconstructed versus actual concentration of each contrast agent is shown in Figs. 5(a) and 5(b) for the La–Gd–Lu and I–Gd–Ho phantoms, respectively. The slopes of each data set were 1.009, 1.019, and 1.017 for La, Gd, and Lu and 0.972, 0.995, and 0.986 for I, Gd, and Ho, respectively. The R^2 values for all data sets were at least 0.996. The difference between the reconstructed and actual concentration in both La–Gd–Lu and I–Gd–Ho phantoms did not exceed 0.25% for all vials.

3.2.2 *Root-mean-square error*

A summary of RMSE values of all vials for each *K*-edge image (Figs. 3 and 4) is shown in Tables 4 and 5 for the La–Gd–Lu and I–Gd-Ho phantoms, respectively. The RMSE values of the zero-contrast vials are also summarized in Tables 4 and 5. For the La–Gd–Lu phantom,

Table 4 RMSE of each vial in all *K*-edge images of the La–Gd–Lu phantom. The RMSE of each vial of contrast agent in its corresponding *K*-edge image is shown in bold; unbolded values are from zero-contrast vials.

	Contrast	RMSE of vial signal (%)			
Concentration		0.5%	1%	3%	5%
La *K*-edge image	**La**	**0.13**	**0.21**	**0.20**	**0.12**
	Gd	0.08	0.02	0.00	0.00
	Lu	0.01	0.00	0.00	0.00
Gd *K*-edge image	La	0.01	0.00	0.00	0.00
	Gd	**0.17**	**0.20**	**0.25**	**0.18**
	Lu	0.12	0.10	0.00	0.00
Lu *K*-edge image	La	0.00	0.00	0.00	0.00
	Gd	0.00	0.00	0.00	0.00
	Lu	**0.29**	**0.36**	**0.36**	**0.51**

Table 5 RMSE of each vial in all *K*-edge images of the I–Gd–Ho phantom. The RMSE of each vial of contrast agent in its corresponding *K*-edge image is shown in bold while unbolded values are from zero-contrast vials.

	Contrast	RMSE of vial signal (%)			
Concentration		0.5%	1%	3%	5%
I *K*-edge image	**I**	**0.11**	**0.21**	**0.21**	**0.12**
	Gd	0.04	0.03	0.00	0.00
	Ho	0.04	0.00	0.00	0.00
Gd *K*-edge image	I	0.06	0.05	0.03	0.03
	Gd	**0.17**	**0.27**	**0.19**	**0.26**
	Ho	0.06	0.05	0.04	0.15
Ho *K*-edge image	I	0.10	0.04	0.00	0.00
	Gd	0.12	0.10	0.18	0.27
	Ho	**0.21**	**0.17**	**0.21**	**0.21**

the highest zero-contrast RMSE value was 0.12% for the Gd *K*-edge image from the 0.5% Lu vial. For the I–Gd–Ho phantom, the highest zero-contrast RMSE value was 0.27% for the Ho *K*-edge image from the 5% Gd vial.

4 Discussion

We have demonstrated simultaneous *K*-edge imaging of high-*Z* contrast agent triplets, five in total, of varying concentrations among four 3D-printed small animal phantoms using a CZT photon-counting detector. For the 3% and 5% concentrations, all contrast agents were detectable in the *K*-edge images. The signals of the 0.5% vials were reconstructed to within their associated error bars as evident in Fig. 5 for all contrast agents studied, albeit it is difficult to detect by eye in

their K-edge images. In the energy-binned CT images, there were not only ring artifacts due to pixel instability but also other streaking artifacts due to the multiple detector position data stitching. These artifacts then propagate from the binned CT images to the K-edge images in Figs. 3 and 4 and decrease image quality. The streaking artifacts were likely caused by the data acquisition timing between multiple detector positions, rather than the precision of the detector positions. Human error was introduced when attempting to start the data acquisition at the exact same time between detector translations, and further timing error by computer lag may have caused variance in the data saving time per acquisition. Since three translations were used to cover the extent of the phantom, a larger active area of the CZT detector that fully covers the data set would reduce both the streaking artifacts and the total acquisition time by a factor of 3 to 4 min. A larger active area would also remove the need for timing accuracy of the data acquisition.

The CZT detector, given the 120-kVp spectrum and the set energy bins, was able to discriminate three contrast agents in the La–Gd–Lu phantom with K-edges 11 keV apart. In addition, there was minimal cross contamination in the peripheral vials in the K-edge images shown in Fig. 3. The CZT detector was able to discriminate three contrast agents in the I–Gd–Ho phantom, two of which had a difference in K-edges of 5.4 keV. The false signal present in the Gd and Ho K-edge images in Fig. 4 was likely caused by the energy resolution of the detector (6 to 9 keV) considering the difference in K-edge energy between Gd and Ho of 5.4 keV. Since the FWHM of the 59.5 keV ^{241}Am gamma ray peak was equal to 8.9 keV, two K-edges a minimum of half the FWHM apart (4.5 keV) near this gamma ray peak energy could be considered as partially resolved in the reconstructed K-edge images. Furthermore, the ability to distinguish Gd and Ho is made possible in part by the weighted K-edge subtraction method. For imaging of Gd (K-edge of 50.2 keV) in the I–Gd–Ho phantom, the COBYLA algorithm determined that there was a large spectral overlap in the 33 to 50 keV ($w_2 = -0.011$) and the 50 to 56 keV ($w_3 = 0.949$) bins and chose to use the 16 to 33 keV ($w_1 = -0.723$) bin instead. Another way to improve this x-ray spectra distinction would be to adjust the energy bin thresholds on the CZT detector such that two thresholds were set to straddle the K-edge energy of a given contrast agent, forming a small energy bin in which the acquired data were discarded. While this approach would likely decrease the amount of cross contamination between contrast agents with similar K-edge energies, it is limited by the number of available energy bins on the CZT detector, which influences the number of contrast agents that could be simultaneously imaged. Intermediate energy bins useful for image reconstruction, in the case of distinguishing Gd and Ho, would decrease in size and suffer from photon starvation effects.

The x-ray beam tube voltage was set to 120 kV and low beam filtration of 1-mm Al was added. This was not an efficient setup from an imaging dose point of view, and future experiments will either consider lowering the tube voltage for imaging of small animal-sized objects or increasing the beam filtration for imaging of larger objects. The 1-mm Al filter, while soft for many preclinical systems, was chosen in this study as thicker beam filtration generally leads to noisier K-edge images of lanthanide contrast agents.[39]

4.1 *Signal Linearity*

For most of the vials, Fig. 5 shows that the signal in each K-edge image is proportional to the concentration. The R^2 values for each data set were above 0.99, suggesting good linearity. This is also supported by the slopes of each linear fit being equal to one within error, except in the cases of Lu and I based on the slope error. The signal in the Lu vials in Figs. 3(c) and 3(f) was especially degraded by the ring artifacts, which may affect the signal linearity.

The signal in each of the 0.5% and 1% vials was more susceptible to degradation by the ring artifacts in the K-edge images. The values of the RMSE in these nonzero contrast vials varied by no more than a factor of 2 compared to the 3% and 5% vials. However, relative to the actual concentration, the RMSE values are drastically higher for lower concentration vials. This suggests the ring artifacts prevent our CZT detector from reconstructing biologically relevant concentrations of contrast agents of <0.1%[31,40] unless a more appropriate ring-artifact correction algorithm is devised. It is evident that the peripheral ring artifacts interfere with the Lu [Figs. 3(c) and 3(f)] vials in their respective K-edge images, as the RMSE values are up to four times higher than the RMSE values of the lower-Z contrast agents with similar concentrations.

The ring artifacts disrupting the Lu vials in the Lu *K*-edge images were likely inflating those RMSE values compared to the other contrast agents in the La–Gd–Lu phantom. The same effect was apparent in the Gd vials in the Gd *K*-edge image of the HC I–Gd–Ho phantom [Fig. 4(c)].

4.2 *Cross Contamination*

As summarized in Table 4, the RMSE of the zero-contrast vials was found to be low (<0.12%) for the La and Lu *K*-edge images, in particular. All zero-contrast RMSE values for the Lu *K*-edge images were 0.00%; this is because in the peripheral zero-contrast ROIs, all values were negative, meaning no Lu signal was present in the La or Gd vials. The same is true in the case of all 3% and 5% zero-contrast vials in the La and Gd *K*-edge images, respectively. The negative pixel values in each zero-contrast ROI were set to 0.

As summarized in Table 5, the RMSE values of the 3% and 5% Gd and Ho vials in the I *K*-edge image were all 0, as described above. The abnormally high RMSE of 0.18% and 0.27% in the 3% and 5% Gd vials, respectively, in the HC Ho *K*-edge image [Fig. 4(c)] suggests the effect of the ring artifacts increasing the signal in the Ho vials. This effect is more apparent for higher concentration Gd vials, as evidenced by the lower RMSE values of 0.12% and 0.10% from the 0.5% and 1% Gd vials in the Ho *K*-edge images. In addition, the next highest RMSE value of 0.15% was from the 5% Ho vial in the HC Gd *K*-edge image. These high RMSE values of Gd and Ho vials in each other's *K*-edge images may also be due to the close difference in *K*-edge energies between Gd and Ho (5.4 keV) compared to the energy response of the CZT detector (6 to 9 keV). Charge sharing from multiple pixel readouts has been shown to account for a degradation in energy resolution.[41] For the high-flux detector used in this study under typical operating conditions (high voltage of 1000 V), we have calculated, based on the previous characterization work,[42,43] that about 40% of photons undergo charge-sharing events that lead to spectral distortion. Fortunately, the detector has built-in anticharge sharing capability[44,45] that rejects those events, and only single count events were analyzed in this study. In this mode of operation, most of the photons that undergo the charge-sharing effect were rejected.

Ring artifacts were especially concentrated in the middle of the HC and LC Lu *K*-edge images [Figs. 3(c) and 3(f)] and the HC Ho *K*-edge image [Fig. 4(c)]. This was the reason for excluding the middle water vial in the RMSE calculations, as no meaningful analysis would be possible.

The weighted summation of the CT images of different energy bins to reconstruct each *K*-edge image utilized the entire PCCT data. Basis material decomposition, as demonstrated in many other PCCT studies using preclinical scanners,[25,28,29,31,46] also uses the entire PCCT data. This method may alleviate some cross contamination between contrast agents and thus decrease the RMSE of each vial. However, one benefit of *K*-edge imaging as opposed to basis material composition is that the mass attenuation coefficient is very similar between contrast agents with similar *Z*s, except for the discontinuity at the *K*-edge energy. The energy threshold windows on photon-counting detectors can be set arbitrarily on either side of the *K*-edge to hone in on the difference of attenuation to maximize the signal. However, beam hardening is an issue for clinical translation that cannot be ignored when imaging human-sized objects. The choice of energy bin thresholds in this study could be better optimized by taking into account beam hardening. In addition, a follow-up study has found that for our current table-top PCCT imaging setup, the optimal energy bin widths should be 10 keV on either side of the Gd *K*-edge energy to maximize *K*-edge contrast-to-noise ratio when imaging only Gd contrast.[39] In the present study, the highest-weighted energy bins that contributed to the formation of Gd *K*-edge images were at least 6 keV wide, since multiple contrast agents were imaged, and therefore, the threshold choice was limited. For the above reasons, this work should be considered as preliminary.

4.3 *Comparison with Previous PCCT Studies*

The prototype CT imaging system from Ref. 27 used a linear CdTe detector array of pixel pitch 0.4 mm and pixel size of ~250 μm, which could not accurately reconstruct 0.3% I and 0.4% Gd for a current exposure of 11.3 mAs. This is compared to the low RMSE (0.11%) of our reconstructed 0.5% I vial in the I–Gd–Ho phantom and higher RMSE (0.17% and 0.17%)

of the 0.5% Gd vials in the La–Gd–Lu and I–Gd–Ho phantoms, respectively. These particular vials were reconstructed to within 0.1% according to Fig. 5. The difference in the reconstruction accuracy of these contrast agents can be attributed to the larger 8-cm-diameter phantom containing slightly larger diameter contrast agent inserts of 8 mm and the difference in imaging setup as outlined above.

The PCCT imaging system from the Si-Mohamed et al. study[18] reconstructed I and Gd concentrations with slopes of 1.04 and 0.98 for a linear fit with an R^2 of 0.99 and 0.98, respectively, using a $400 \times 400 \times 250$ μm^3 voxel grid. This is to compare with our Gd slope values of 1.019 and 0.995 for both the La–Gd–Lu and I–Gd–Ho phantoms, and our I slope of 0.972 with a smaller reconstructed cubic voxel size of 250 μm. Our RMSE of the Gd K-edge image from I vials only ranged between 0.03% and 0.06%, compared to 0.33% from Ref. 18 meaning our Gd K-edge images suffered from less I cross contamination. Aside from the larger phantom size with a quoted CT dose index of 0.74 mGy and larger vial size, the energy thresholds on the prototype photon-counting detector used in Ref. 18 were optimized for each of the separate scans of each contrast agent and differed from the energy thresholds used in our experiment.

The Panta et al. study[28] simultaneously imaged I, Gd, and gold using a preclinical CdTe-Medipix3RX photon-counting detector with a pixel pitch of 110 μm and four optimized energy bins. Using an ordered-subset expectation maximization iterative image reconstruction and basis material decomposition to reconstruct images with a cubic voxel size of 180 μm, 0.2% Gd and 0.9% I solutions were identified in the K-edge images. According to Fig. 5, our imaging system underestimated the concentration of the 1% I by 0.2%. However, the 0.5% Gd vials in the LC La–Gd–Lu and I–Gd–Ho phantoms were reconstructed to within 0.1%. Our imaging system is consistent with Ref. 28 when imaging similar concentrations of Gd.

To our knowledge, La, Lu, and Ho contrast agents have not been imaged previously using PCCT. Ytterbium also belongs to the lanthanide group and has been imaged with PCCT. The Pan et al. study[24] used PCCT to image ytterbium ($Z = 70$, K-edge energy = 61.3 keV) nanoparticulates *in vivo*. With their preclinical CZT detector, Pan et al.[24] reconstructed a single slice image of ytterbium nanoparticulates using basic material decomposition at a concentration of 0.01% by weight. A fraction of this concentration in the heart was detectable in a mouse with a reconstructed pixel size of 100 μm. The 0.5% Lu vial ($Z = 71$, K-edge energy = 63.3 keV) in our LC La–Gd–Lu phantom was visible in the K-edge image and reconstructed to within <0.1% according to Fig. 5 with a high RMSE of 0.29%. While a direct comparison is difficult to perform, the difference in visibility can be attributed to the need for energy bin optimization and different reconstruction methods when imaging Lu simultaneously with other contrast agents.

In our setup employing a continuous x-ray beam, the total dose was 624 mGy over a total scan time of 12 min or 242 s. This dose is what the phantom received, and it is an unacceptably high dose for living animals.[47] The CZT detector acquired 180 projection images in 0.25-s periods for image reconstruction, which resulted in a true acquisition time of only 45 s of the 242-s scan. The achievable imaging dose was therefore calculated to be 116 mGy ($45\ s \times 624\ mGy/242\ s$). The total dose could be decreased by a variety of different scanning strategies such as by employing a pulsed beam synchronized with the detector acquisition with a duty cycle or by reducing the beam current while acquiring projection images in longer periods. Alternatively, the rotation speed could be increased while keeping the same beam current, which would then result in spatial blurring of the image.

5 Conclusions

We have simultaneously imaged three contrast agents in a small animal-sized phantom; the clinically relevant I and Gd in combination with novel lanthanide contrast agents, such as La, Lu, and Ho. This was achieved using weighted K-edge subtraction imaging with a CZT detector with six energy bins capable of sustaining high count rates. This first demonstration of multiplexed PCCT imaging of similar-Z contrast agents, with a difference of Z as low as 3 and K-edge energy as low as 5.4 keV, on a table-top imaging system could lead to improved disease diagnosis with novel contrast agents.

Disclosures

Redlen Technologies Inc. provided the CZT detector in the presented work.

Acknowledgments

The authors would like to thank the Redlen Technologies team for their support and advice on data acquisition, Dylan Y. Breitkreutz for simulating the x-ray tube beam, Nolan Esplen for assistance with dose measurements, and Logan Francis for assistance with data presentation. We would like to thank Dr. Elmaddin Guliyev of Redlen Technologies Inc. for performing some of the detector measurements. The authors acknowledge Canada Foundation for Innovation and British Columbia Knowledge Development Fund for their funding for the table-top x-ray system. The presented work was supported by NSERC Discovery Grants, Engage and Engage Plus, and the Canada Research Chairs program.

References

1. R. E. Alvarez and A. Macovski, "Energy-selective reconstructions in x-ray computerised tomography," *Phys. Med. Biol.* **21**(5), 733–744 (1976).
2. T. R. C. Johnson et al., "Material differentiation by dual energy CT: initial experience," *Eur. Radiol.* **17**, 1510–1517 (2007).
3. N. Takahashi et al., "Dual-energy CT iodine-subtraction virtual unenhanced technique to detect urinary stones in an iodine-filled collecting system: a phantom study," *Am. J. Roentgenol.* **190**(5), 1169–1173 (2008).
4. S. F. Thieme et al., "Dual-energy CT for the assessment of contrast material distribution in the pulmonary parenchyma," *Am. J. Roentgenol.* **193**(1), 144–149 (2009).
5. D. H. Lee et al., "Dual-energy CT iodine quantification for characterizing focal thyroid lesions," *Head Neck* **41** (2018).
6. J. Fornaro et al., "Dual-and multi-energy CT: approach to functional imaging," *Insights Imaging* **2**(2), 149–159 (2011).
7. C. H. McCollough et al., "Dual-and multi-energy CT: principles, technical approaches, and clinical applications," *Radiology* **276**(3), 637–653 (2015).
8. M. Bazalova et al., "Investigation of x-ray fluorescence computed tomography (XFCT) and K-edge imaging," *IEEE Trans. Med. Imaging* **31**(8), 1620–1627 (2012).
9. A. Pourmorteza et al., "Abdominal imaging with contrast-enhanced photon-counting CT: first human experience," *Radiology* **279**(1), 239–245 (2016).
10. R. Symons et al., "Feasibility of dose-reduced chest CT with photon-counting detectors: initial results in humans," *Radiology* **285**(3), 980–989 (2017).
11. R. Symons et al., "Photon-counting CT for simultaneous imaging of multiple contrast agents in the abdomen: an *in vivo* study," *Med. Phys.* **44**(10), 5120–5127 (2017).
12. D. Muenzel et al., "Spectral photon-counting CT: initial experience with dual-contrast agent K-edge colonography," *Radiology* **283**(3), 723–728 (2017).
13. N. G. Anderson and A. P. Butler, "Clinical applications of spectral molecular imaging: potential and challenges," *Contrast Media Mol. Imaging* **9**(1), 3–12 (2014).
14. A. C. Silva et al., "Dual-energy (spectral) CT: applications in abdominal imaging," *RadioGraphics* **31**(4), 1031–1046 (2011).
15. D. S. Gierada and K. T. Bae, "Gadolinium as a CT contrast agent: assessment in a porcine model," *Radiology* **210**(3), 829–834 (1999).
16. K. Taguchi, "Imaging technologies and potential clinical applications of photon-counting x-ray computed tomography," in *Radiation Detectors for Medical Imaging*, J. S. Iwancyzk, Ed., pp. 149–168, CRC Press, Boca Raton, Florida (2015).
17. J. Bennett et al., "Hybrid spectral micro-CT: system design, implementation, and preliminary results," *IEEE Trans. Biomed. Eng.* **61**(2), 246–253 (2014).
18. S. Si-Mohamed et al., "Multicolour imaging with spectral photon-counting CT: a phantom study," *Eur. Radiol. Exp.* **2**(1), 34 (2018).

19. S. Feuerlein et al., "Multienergy photon-counting K-edge imaging: potential for improved luminal depiction in vascular imaging," *Radiology* **249**(3), 1010–1016 (2008).
20. M. S. Joy et al., "Randomized, double-blind, placebo-controlled, dose-titration, phase III study assessing the efficacy and tolerability of lanthanum carbonate: a new phosphate binder for the treatment of hyperphosphatemia," *Am. J. Kidney Diseases* **42**(1), 96–107 (2003).
21. R. R. Allison and C. H. Sibata, "Oncologic photodynamic therapy photosensitizers: a clinical review," *Photodiagn. Photodyn. Ther.* **7**(2), 61–75 (2010).
22. X. Zhang et al., "Design and regulation of $NaHoF_4$ and $NaDyF_4$ nanoparticles for high-field magnetic resonance imaging," *Chem. Mater.* **28**(9), 3060–3072 (2016).
23. P. F. FitzGerald et al., "CT image contrast of high-Z elements: phantom imaging studies and clinical implications," *Radiology* **278**(3), 723–733 (2016).
24. D. Pan et al., "An early investigation of ytterbium nanocolloids for selective and quantitative 'multicolor' spectral CT imaging," *ACS Nano* **6**(4), 3364–3370 (2012).
25. F. Ostadhossein et al., "Multi-'color' delineation of bone microdamages using ligand-directed sub-5 nm hafnia nanodots and photon counting CT imaging," *Adv. Funct. Mater.* **30**(4), 1–12 (2020).
26. H. Ghadiri et al., "K-edge ratio method for identification of multiple nanoparticulate contrast agents by spectral CT imaging," *Br. J. Radiol.* **86**(1029), 20130308 (2013).
27. J. Schlomka et al., "Experimental feasibility of multi-energy photon-counting K-edge imaging in pre-clinical computed tomography," *Phys. Med. Biol.* **53**(15), 4031 (2008).
28. R. Panta et al., "Element-specific spectral imaging of multiple contrast agents: a phantom study," *J. Instrum.* **13**(2), T02001 (2018).
29. M. Moghiseh et al., "Discrimination of multiple high-Z materials by multi-energy spectral CT: a phantom study," *JSM Biomed. Imaging Data Pap.* **61**, 1007 (2016).
30. J. F. Butler et al., "$Cd_{1-x}Zn_xTe$ detector imaging array," *Proc. SPIE* **1896**, 30–38 (1993).
31. S. Si-Mohamed et al., "Spectral photon-counting computed tomography (SPCCT): *in-vivo* single-acquisition multi-phase liver imaging with a dual contrast agent protocol," *Sci. Rep.* **9**(1), 8458 (2019).
32. K. Iniewski, "CZT sensors for computed tomography: from crystal growth to image quality," *J. Instrum.* **11**(12), C12034 (2016).
33. J. H. Hubbell and S. M. Seltzer, "Tables of x-ray mass attenuation coefficients and mass energy-absorption coefficients 1 kev to 20 Mev for elements Z = 1 to 92 and 48 additional substances of dosimetric interest," Technical Report, National Inst. of Standards and Technology-PL, Gaithersburg, Maryland, United States Department of Commerce, Technology Administration, National Institute of Standards and Technology (1996), updated 2004 Jul.
34. D. Y. Breitkreutz et al., "Experimental demonstration of the skin sparing ability of a proof-of-principle kilovoltage arc therapy system," In preparation (2020).
35. B. Münch et al., "Stripe and ring artifact removal with combined wavelet–Fourier filtering," *Opt. Express* **17**(10), 8567–8591 (2009).
36. L. A. Feldkamp, L. Davis, and J. W. Kress, "Practical cone-beam algorithm," *J. Opt. Soc. Am. A* **1**(6), 612–619 (1984).
37. M. J. Powell, "A direct search optimization method that models the objective and constraint functions by linear interpolation," in *Advances in Optimization and Numerical Analysis*, S. Gomez and J. P. Hennart, Eds., pp. 51–67, Springer, Dordrecht (1994).
38. P. Virtanen et al., "SciPy 1.0: fundamental algorithms for scientific computing in Python," *Nat. Methods* **17**, 261–272 (2020).
39. D. Richtsmeier et al., "Parameter optimization for multi-contrast imaging using photon-counting CT," Submitted to *J. Med. Imaging* (2020).
40. D. P. Cormode et al., "Multicolor spectral photon-counting computed tomography: in vivo dual contrast imaging with a high count rate scanner," *Sci. Rep.* **7**(1), 1–11 (2017).
41. J. C. Kim et al., "Charge sharing in common-grid pixelated CdZnTe detectors," *Nucl. Instrum. Methods Phys. Res. Sec. A* **654**(1), 233–243 (2011).
42. M. Veale et al., "Measurements of charge sharing in small pixel CdTe detectors," *Nucl. Instrum. Methods Phys. Res. Sec. A* **767**, 218–226 (2014).

43. B. Thomas et al., "Characterisation of Redlen high-flux CdZnTe," *J. Instrum.* **12**(12), C12045 (2017).
44. K. Iniewski, M. C. Veale, and M. Bazalova-Carter, "High-flux CZT for new Frontiers in computed tomography (CT), non-destructive testing (NDT) and high-energy physics," in *IEEE Nuclear Sci. Symp. and Med. Imaging Conf.*, Manchester (2019).
45. K. Iniewski et al., "Performance characteristics of 250+ Mcps/mm^2 CZT detector module for spectral computed tomography," in *Workshop Med. Appl. Spectrosc. X-Ray Detectors*, CERN (2019).
46. M. Persson et al., "Energy-resolved CT imaging with a photon-counting silicon-strip detector," *Phys. Med. Biol.* **59**(22), 6709 (2014).
47. J. M. Boone, O. Velazquez, and S. R. Cherry, "Small-animal x-ray dose from micro-CT," *Mol. Imaging* **3**(3), 153535002004041 (2004).

Chelsea A. S. Dunning is a PhD candidate in the Department of Physics and Astronomy at the University of Victoria. She received her BSc degree in Honours Physics from the University of British Columbia in 2015. Her current research interests include photon-counting computed tomography, x-ray fluorescence computed tomography, and detector optimization for preclinical imaging systems.

Jericho O'Connell is a Master's student in the Department of Physics and Astronomy at the University of Victoria. His current research interests include photon-counting computed tomography, FLASH radiotherapy, and detector optimization for mega-voltage portal imaging.

Frank C. J. M. Van Veggel obtained his MEng in 1986 and his PhD in 1990, and joined the company Akzo Nobel. In 1992 he began performing research in Prof. Reinhoudt's group at the University of Twente. Two paradigm-shifting articles were published in 2002. In 2002 he accepted a Tier II Canada Research Chair at the University of Victoria, renewed in 2007. In 2015 he became a member of the Royal Society of Canada.

Krzysztof (Kris) Iniewski is managing R&D development activities at Redlen Technologies Inc., a detector company based in BC, Canada. Prior to Redlen, Kris held various management and academic positions at PMC-Sierra, University of Alberta, SFU, UBC, and University of Toronto. Dr. Iniewski has published 150+ research papers in international journals and conferences and holds 20+ international patents. He wrote and edited several books for Wiley, Cambridge University Press, Mc-Graw Hill, CRC Press, and Springer.

Magdalena Bazalova-Carter is an Assistant Professor and Tier 2 Canada Research Chair in Medical Physics in the Department of Physics and Astronomy at the University of Victoria in British Columbia, Canada. She received her PhD degree at McGill University and postdoctoral training at Stanford University. Her current research interests include Monte Carlo simulations and experiments of x-ray fluorescence and photon-counting CT imaging, small animal radiotherapy, and FLASH radiotherapy.

Biographies of the other authors are not available.